

Non-linear dynamics of spinning bosonic stars: formation and stability

N. Sanchis-Gual,¹ F. Di Giovanni,² M. Zilhão,¹ C. Herdeiro,¹ P. Cerdá-Durán,² J. A. Font,^{2,3} and E. Radu⁴

¹*Centro de Astrofísica e Gravitação - CENTRA,
Departamento de Física, Instituto Superior Técnico - IST,
Universidade de Lisboa - UL, Avenida Rovisco Pais 1, 1049-001, Portugal*

²*Departamento de Astronomía y Astrofísica, Universitat de València,
Dr. Moliner 50, 46100, Burjassot (València), Spain*

³*Observatori Astronòmic, Universitat de València,
C/ Catedrático José Beltrán 2, 46980, Paterna (València), Spain*

⁴*Departamento de Física da Universidade de Aveiro and Centre for Research and Development
in Mathematics and Applications (CIDMA), Campus de Santiago, 3810-183 Aveiro, Portugal*

(Dated: July 2019)

We perform numerical evolutions of the fully non-linear Einstein–(complex, massive) Klein-Gordon and Einstein–(complex) Proca systems, to assess the formation and stability of spinning bosonic stars. In the scalar/vector case these are known as boson/Proca stars. Firstly, we consider the formation scenario. Starting with constraint-obeying initial data, describing a dilute, axisymmetric cloud of spinning scalar/Proca field, gravitational collapse towards a spinning star occurs, via gravitational cooling. In the scalar case the formation is transient, even for a non-perturbed initial cloud; a non-axisymmetric instability always develops ejecting all the angular momentum from the scalar star. In the Proca case, by contrast, no instability is observed and the evolutions are compatible with the formation of a spinning Proca star. Secondly, we address the stability of an existing star, a stationary solution of the field equations. In the scalar case, a non-axisymmetric perturbation develops collapsing the star to a spinning black hole. No such instability is found in the Proca case, where the star survives large amplitude perturbations; moreover, some excited Proca stars decay to, and remain as, fundamental states. Our analysis suggests bosonic stars have different stability properties in the scalar/vector case, which we tentatively relate to their toroidal/spheroidal morphology. A parallelism with instabilities of spinning fluid stars is briefly discussed.

Introduction. Recent data from gravitational-wave astronomy [1], as well as from electromagnetic VLBI observations near galactic centres [2, 3], support the black hole (BH) *hypothesis*: BHs commonly populate the Cosmos, with masses spanning a range of (at least) 10 orders of magnitude. Yet, the elusiveness of the event horizon, the defining property of a BH, rules out an observational “proof” of their existence. Considering, thus, models of BH mimickers is a valuable tool to understand the uniqueness of BH phenomenology.

Within the landscape of BH mimickers, bosonic stars (BSs) are particularly well motivated. They arise in simple and physically sound field theoretical models: complex, massive, bosonic fields (scalar [4, 5] or vector [6]) minimally coupled to Einstein’s gravity. Dynamically, moreover, *static, spherical* BSs, are viable; for some range of parameters, the lowest energy stars - *the fundamental family* (FF) - have a formation mechanism [7, 8] and are perturbatively stable [6, 9–11]. The properties and phenomenology of such static BSs have been considered at length (see *e.g.* the reviews [12, 13]), including dynamical situations such as orbiting binaries, from which gravitational waveforms have been extracted [14–16]. These studies unveiled a close parallelism in the phenomenology of spherical BSs, regardless of their scalar or vector nature.

Astrophysically, however, rotation is ubiquitous and

should, thus, be included in more realistic models of BSs. Both scalar [17–19] and vector [6, 20] *axisymmetric, spinning* BSs (SBSs) have been constructed and some of their phenomenology has been studied [21, 22]. Yet, their dynamical and stability properties, a key aspect of their physical viability, have remained essentially unexplored - see the discussion in [23].

In this letter we describe the dynamical properties of SBSs, obtained from fully non-linear numerical simulations of the corresponding Einstein-matter system. We provide evidence that scalar SBSs in the FF are prone to a non-axisymmetric instability. Thus, such stars are transient states, in a dynamical formation scenario. Assuming an already formed scalar SBS, on the other hand, it collapses into a BH after a non-axially symmetric instability develops. Vector SBSs (*aka* spinning Proca stars), by contrast, are dynamically robust. In the formation scenario we find no evidence of an instability. In agreement, for already formed vector SBSs we observe that: (*i*) even large perturbations are dissipated away; and (*ii*) some stars in excited families decay to the FF where they remain. This suggests scalar/vector SBSs have different dynamical properties and viability, and their toroidal/spheroidal morphology provides a suggestive interpretation.

SBSs as stationary solutions. Scalar and vector BSs, with and without spin, arise as equilibrium states

in models with Lagrangian density $\mathcal{L} = R/(16\pi G) + \mathcal{L}_m$, where R is the Ricci scalar, G is Newton's constant and

$$\mathcal{L}_m = -\partial^\alpha \phi \partial_\alpha \bar{\phi} - \mu^2 \phi \bar{\phi}, \quad \mathcal{L}_m = -\frac{\mathcal{F}_{\alpha\beta} \bar{\mathcal{F}}^{\alpha\beta}}{4} - \frac{\mu^2}{2} \mathcal{A}_\alpha \bar{\mathcal{A}}^\alpha, \quad (1)$$

describe the scalar and vector cases, respectively. The scalar (ϕ) and vector (\mathcal{A}_α) fields are complex-valued, with conjugation denoted by an overbar, both with mass μ . As usual, $\mathcal{F} = d\mathcal{A}$. Henceforth, units with $G = 1 = c = \mu$ are used.

Scalar SBSs were first constructed numerically in [17, 18], as asymptotically flat, stationary and axisymmetric solutions of the above Einstein-Klein-Gordon system. They are a ‘‘mass torus’’ in general relativity - Fig. 1 (left panel). Scalar SBSs form a discrete set of families of continuous solutions. Each family is labelled by two integers: m , the azimuthal winding number and n , the node (or overtone) number, see *e.g.* [12, 13, 19, 24, 25]. The FF, which has the lowest energy, has $(m, n) = (1, 0)$. Fixing the family, *i.e.* (m, n) , SBS are characterised by their total mass M and angular momentum J . They form a one-dimensional set, often labelled by M , and oscillation frequency, ω . The (dynamically) most interesting solutions occur in between the Newtonian limit, $\omega \rightarrow 1$ and $M \rightarrow 0$, and the maximal mass solution. The latter occurs for $\omega \rightarrow \omega_{M_{\max}} (\simeq 0.775$ for the FF) and the ADM mass becomes highest, $M \rightarrow M_{\max} (\simeq 1.315$ for the FF). In Table I we list the properties of two illustrative scalar SBSs used in the simulations below.

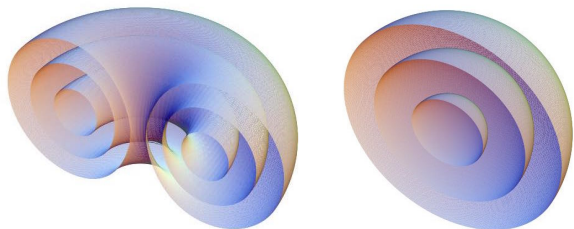


FIG. 1: Surfaces of constant energy density for illustrative SBSs: (left panel) scalar configuration 2_S ; (right panel) vector configuration 1_P . The toroidal *vs.* spheroidal nature is clear.

Configuration	1_S	2_S	1_P	2_P	3_P	4_P	5_P
type (S or P)	S	S	P	P	P	P	P
n	0	0	0	0	1	1	1
ω	0.90	0.83	0.95	0.90	0.95	0.90	0.85
M	1.119	1.281	0.534	0.726	1.149	1.456	1.564
J	1.153	1.338	0.543	0.750	1.171	1.500	1.622

TABLE I: Physical properties of some illustrative SBSs. The second row identifies if they are scalar (S) or vector/Proca (P). All solutions have $m = 1$ and none has an ergo-region.

Vector SBSs were first reported as excited states ($n = 1$) in [6, 20]. The FF was considered in [26, 27]. The aforementioned description for scalar SBSs applies, *mutatis mutandis*. An important distinction, however, is that the energy distribution is now spheroidal, rather than toroidal [27] - Fig. 1 (right panel). Moreover, for the FF, $\omega_{M_{\max}} \simeq 0.562$ and $M_{\max} \simeq 1.125$ [27]. For the excited family with $(m, n) = (1, 1)$, $\omega_{M_{\max}} \simeq 0.839$ and $M_{\max} \simeq 1.568$ [6]. In Table I we list the properties of two [three] representative vector SBSs, in the FF $[(m, n) = (1, 1)]$ family).

Dynamical formation of SBSs. In the spherical case, numerical simulations established that both scalar [7] and vector [8] BSs form dynamically, from a spherical ‘‘cloud’’ of dilute scalar or vector field. The cloud collapses due to its self-gravity. The ejection of energetic scalar or vector ‘‘particles’’, dubbed gravitational cooling, allows the formation of a compact object.

For studying the formation of SBSs, with $m = 1$, the Hamiltonian, momentum and (in the vector case) Gauss constraint are solved by appropriately choosing a Gaussian radial dependence for the key variables, together with a non-spherical profile (see Appendix A). For the scalar case the ‘‘matter’’ initial data is:

$$\phi(t, r, \theta, \varphi) = A r e^{-\frac{r^2}{\sigma^2}} \sin \theta e^{i(\varphi - \omega t)}, \quad (2)$$

where A, σ are constants and $e^{-i\omega t}$ is the harmonic dependence. Besides this unperturbed initial data, we also evolve perturbed initial data of two types: replacing in (2) $e^{i\varphi} \rightarrow e^{i\varphi}(1 + A_1 \cos(2\varphi))$; or, alternatively, replacing $e^{i\varphi} \rightarrow e^{i\varphi} + A_2 e^{2i\varphi}$. A_1, A_2 are the amplitudes of the perturbations.

Fully non-linear numerical evolutions of the Einstein-matter system using this initial data were carried out with the EINSTEIN TOOLKIT [28, 29] - see Appendix B. Two choices of A were considered, both of which yield global data for the scalar cloud ($M_{\text{Sc}}, J_{\text{Sc}}$) close to that of equilibrium scalar SBS solutions. The first/second choices give $M_{\text{Sc}}^{(1)} \sim 0.46 \sim J_{\text{Sc}}^{(1)}$, and $M_{\text{Sc}}^{(2)} \sim 0.89 \sim J_{\text{Sc}}^{(2)}$, respectively. We have run simulations with both perturbed and unperturbed initial data, with $A_1 = 0, 0.001, 0.01, 0.05$ and $A_2 = 0, 0.05$. Typically, $\sigma = 40$.

All evolutions show the emergence of a non-axisymmetric instability. The time at which the instability kicks in depends on the type and amplitude of the perturbation; but even the lowest mass unperturbed model ($M_{\text{Sc}}^{(1)}$) exhibits non-axisymmetric features at a sufficiently long time scale ($t \sim \mathcal{O}(10^4)$). The instability generically triggers a larger ejection of angular momentum than mass, reshaping the toroidal energy distribution into a spherical one. This suggests that the asymptotic end state of the cloud evolution is either a spherical (non-spinning) scalar BS or even, merely, ejected debris carrying all angular momentum and energy.

As an illustration, Fig. 2 exhibits snapshots of the

equatorial plane evolution of the energy density, ρ_E (left panels) and angular momentum density, ρ_J (middle-left panels), for the unperturbed scalar initial data with mass $M_{\text{Sc}}^{(2)}$ [51]. Initially, the collapse preserves axial symmetry. Around $t \sim 4000$, however, the non-axisymmetric

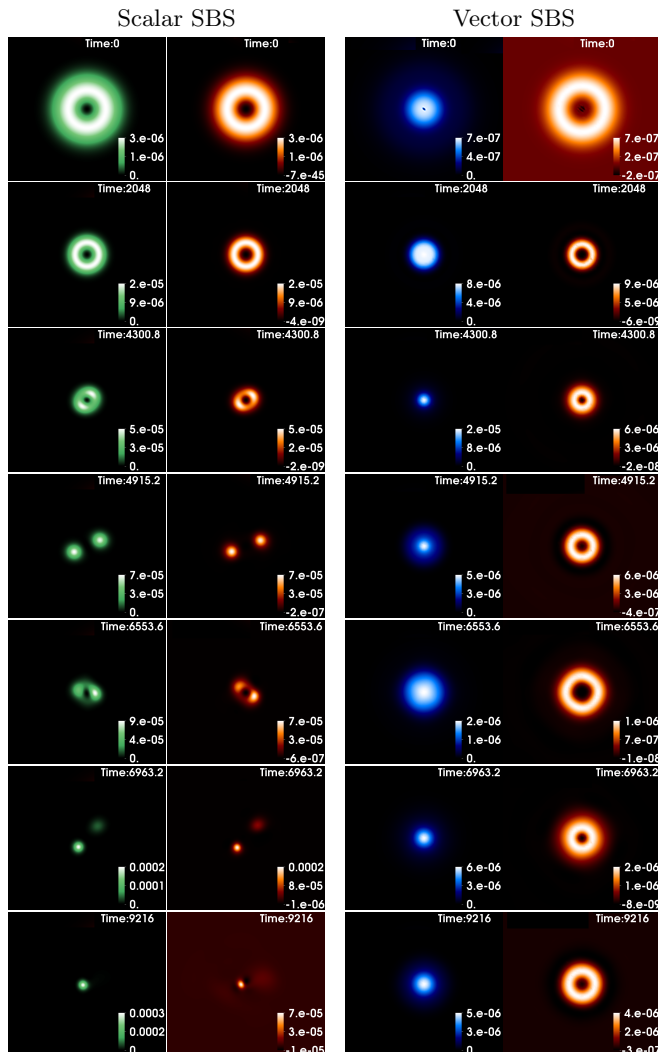


FIG. 2: Time evolution of an equatorial cut of ρ_E (blue/green) and ρ_J (orange) in the formation scenario of a scalar (left side) or a vector (right side) SBS.

instability is visible, producing a fragmentation event: the star splits into a roughly symmetric orbiting binary. The binary is, nonetheless, bound and recollapses to a deformed spinning star, around $t \sim 6500$. This star breaks into two asymmetric pieces, which again recollapse into a spheroidal star with angular momentum. Around $t \sim 10000$, this residual, still evolving, star has $(M, J) = (0.49, 0.16)$, evaluated up to $r = 30$, and an oscillation frequency $\omega \sim 0.96$. For this ω , the FF static scalar BS has $(M, J) = (0.45, 0)$. Thus, this (or a neighbour) static scalar BS appears to be asymptotically approached, after the remaining J is shed away.

Now consider the formation of a vector SBS. The construction of initial data is more complex due to the Gauss constraint [8, 30]. After a 3+1 splitting of \mathcal{A}_μ , the key variables are the scalar and 3-vector potentials together with the electric field. The first of these admits a solution almost identical to (2), but the others are more involved - Appendix A. These initial data can again be perturbed. We have considered a perturbation analogous to the first type considered in the scalar case; the perturbation amplitudes studied were $A_1 = A_2 = 0, 0.05$. Initial data describing a Proca cloud with three different values of global data were used: $M_{\text{Pc}}^{(1)} \sim 0.46 \sim J_{\text{Pc}}^{(1)}$, $M_{\text{Pc}}^{(2)} \sim 0.56 \sim J_{\text{Pc}}^{(2)}$ and $M_{\text{Pc}}^{(3)} \sim 0.77 \sim J_{\text{Pc}}^{(3)}$.

The unperturbed models evolutions are instability-free during the simulations, lasting up to $t \sim 10^4$. This is illustrated by the 3rd and 4th columns in Fig. 2 which show snapshots of the time evolution of the unperturbed Proca cloud $M_{\text{Pc}}^{(2)}$. The gravitational collapse ejects part of the mass and angular momentum, which shows the gravitational cooling mechanism at play. At $t \sim 10^4$ the star has $(M, J) = (0.35, 0.38)$, evaluated up to $r = 60$, and $\omega \sim 0.985$. For this ω , the FF vector SBS has $(M, J) = (0.301, 0.303)$. Thus, this (or a neighbour) vector SBS appears to be asymptotically approached. For the perturbed initial Proca clouds, on the other hand, the energy density oscillates strongly. Nonetheless, no sudden loss of angular momentum is observed, which suggests the endpoint is still a vector SBS.

Evolution of equilibrium SBSs. The dichotomy observed in the formation scenario can be further assessed by considering the dynamics of SBSs obtained as equilibrium solutions of the corresponding Einstein-matter system. A perturbative stability analysis of these SBSs, such as the ones in [6, 9, 10] for the spherical case, seems challenging. Thus, we resort to non-linear numerical evolutions of the Einstein-matter system, analogue to the ones in the formation scenario, but now starting with the equilibrium solutions as initial data. This generalises the evolutions in [31] for non-spinning BSs.

First consider the scalar SBSs. Fig. 3 shows the time evolution of model 2_S . Up to $t \sim 1000$ the star remains essentially undisturbed; then, following the development of a non-axisymmetric perturbation, see upper panels, the star pinches off into two fragments. The resulting binary is gravitationally bound and collapses into a BH at $t \sim 1200$. This is diagnosed by both the appearance of an apparent horizon (AH), whose mass is shown in the main panel, and the vanishing of the lapse function, α , as seen in the inset of Fig. 3. A similar evolution is observed for model 1_S . This confirms that scalar SBSs, even in the FF, are prone to a non-axisymmetric instability. Unlike the formation scenario, here the instability leads to a complete gravitational collapse, likely due to the more compact initial data.

The behaviour of the vector SBSs is distinct. FF solu-

using constraint-abiding initial data. A related question pertains the impact of matter self-interactions in the dynamics reported herein.

Acknowledgements. We thank Carlos Palenzuela, Darío Núñez, Juan Carlos Degollado, and Sergio Gimeno-Soler, for useful discussions and valuable comments. This work has been supported by the Spanish MINECO (grant AYA2015-66899-C2-1-P), by the Generalitat Valenciana (ACIF/2015/216), by the Fundação para a Ciência e a Tecnologia (FCT) projects PTDC/FIS-OUT/28407/2017, UID/MAT/04106/2019 (CIDMA) and UID/FIS/00099/2013 (CENTRA), by national funds (OE), through FCT, I.P., in the scope of the framework contract foreseen in the numbers 4, 5 and 6 of the article 23, of the Decree-Law 57/2016, of August 29, changed by Law 57/2017, of July 19. This work has further been supported by the European Union’s Horizon 2020 research and innovation (RISE) programmes H2020-MSCA-RISE-2015 Grant No. StronGrHEP-690904 and H2020-MSCA-RISE-2017 Grant No. FunFiCO-777740. We would like to acknowledge networking support by the COST Action GWverse CA16104. MZ acknowledges financial support provided by FCT/Portugal through the IF programme, grant IF/00729/2015. PC acknowledges the Ramon y Cajal funding (RYC-2015-19074) supporting his research. Computations have been performed at the Servei d’Informàtica de la Universitat de València, on the “Baltasar Sete-Sois” cluster at IST, and at MareNostrum (via PRACE Tier-0 Grant No. 2016163948).

Appendix A. Initial data and numerical evolutions. To perform numerical relativity evolutions, one must construct an initial configuration for the spacetime and matter fields that satisfies all the Einstein constraint equations. We solve numerically the Hamiltonian and momentum constraints using the extended conformally flatness condition (XCFC) approximation [40]. For fast rotating neutron stars XCFC has been shown to provide accurate space-times within 1% of full GR. In the following we sketch the main steps for our application.

In the $3 + 1$ spacetime decomposition the metric can be expressed as

$$g_{\mu\nu} dx^\mu dx^\nu = -\alpha^2 dt^2 + \gamma_{ij} (dx^i + \beta^i dt)(dx^j + \beta^j dt), \quad (3)$$

where α is the lapse function, and β^i is the shift vector. We apply a conformal decomposition of the spatial 3-metric

$$\gamma_{ij} = \Psi^4 \tilde{\gamma}_{ij}, \quad (4)$$

where Ψ is the conformal factor. In XCFC, $\tilde{\gamma}_{ij}$ is approximated by the flat 3-metric, that simplifies notably the constraint equations. The procedure we follow to solve the constraints is the following.

1. Make an ansatz for the matter fields (which we will detail below for the scalar and vector case).
2. Set the geometry, as a first step, to be Minkowski spacetime: $\alpha = \Psi = 1$ and $\beta^i = 0$. Then evaluate the matter source terms in the Hamiltonian and momentum constraints.
3. Having obtained the matter source terms, solve the constraint equations, obtaining an improved (non-Minkowski) value for α , Ψ and β^i .
4. With the updated values for the metric quantities, evaluate again the matter fields and matter source terms. Then, repeat the procedure iteratively.

At each iteration, we evaluate the L2-norm of the difference between the updated and the previous step values. If it is lower than a certain tolerance (10^{-8}), we consider it has converged to a constraint-satisfying solution.

Let us now consider in detail the ansatz for both the scalar and Proca field, and the explicit form of the matter source terms.

Scalar case

The evolution formulation adopted is the one described in [41], which involves the scalar field ϕ and the conjugated momenta Π defined as

$$\Pi = -\frac{1}{\alpha} (\partial_t - \beta^i \partial_i) \phi. \quad (5)$$

We specify the “shape” of the scalar cloud as

$$\phi(t, r, \theta, \varphi) = R(r) Y_{11}(\theta, \varphi) e^{-i\omega t}, \quad (6)$$

where $Y_{11}(\theta, \varphi) = \sin \theta e^{i\varphi}$ is the $\ell = m = 1$ spherical harmonic and $R(r) = A r e^{-\frac{r^2}{\sigma^2}}$. At $t = 0$,

$$\Pi = -\frac{i}{\alpha} (\omega + \beta^\varphi) \phi, \quad (7)$$

where we use that β^φ is the only non-zero component of the shift vector, a consequence of the axisymmetry invariance of the energy-momentum tensor. Note that the definition of $R(r)$ includes a factor r that cancels out the $1/r^2$ factors appearing in the matter source terms, due to the spherical spatial coordinates, and yields a well-defined behaviour in the limit $r \rightarrow 0$.

Proca case

The evolution formulation adopted is the one described in [30], which involves the scalar potential \mathcal{X}_ϕ , the vector potential \mathcal{X}_i and the “electric” and “magnetic” fields E^i and $B^i = \epsilon^{ijk} D_j \mathcal{X}_k$, where D_i is the spatial covariant derivative and ϵ^{ijk} is the anti-symmetric Levi-Civita

symbol. In the Proca case, besides solving the Hamiltonian and momentum constraints, it is necessary to solve the Gauss constraint which reads

$$D_i E^i = -\mu^2 \mathcal{X}_\phi . \quad (8)$$

We assume E^i is conservative; thus it is the gradient of a potential V , $E^i = -\nabla^i V$. In this way, the Gauss constraint becomes

$$\nabla^2 V = \mu^2 \mathcal{X}_\phi . \quad (9)$$

Now, the ansatz for the scalar potential is chosen to be

$$\mathcal{X}_\phi(t, r, \theta, \varphi) = R(r) Y_{11}(\theta, \varphi) e^{-i\omega t} , \quad (10)$$

where $R(r) = A r^2 e^{-\frac{r^2}{\sigma^2}}$, and we solve equation (9) to obtain V and, thus, E^i . Due to the fact that the spherical harmonics $Y_{lm}(\theta, \varphi)$ are eigenfunctions of the operator $r^2 \nabla^2$ with eigenvalues $-\ell(\ell+1)$, Eq. (9) can be reduced to an ordinary differential equation which depends only on the radial part and reads, at $t = 0$,

$$\frac{1}{r} \partial_r^2 [r V(r)] - \frac{2}{r^2} V(r) = \mu^2 R(r) . \quad (11)$$

Similarly to the scalar case, the r^2 factor in $R(r)$ is needed to have a well-defined behaviour in the limit $r \rightarrow 0$. We solve Eq. (11) analytically specifying boundary conditions $\lim_{r \rightarrow 0} V(r) = 0$ and $\lim_{r \rightarrow \infty} V(r) = 0$ to find

$$V(r) = \frac{A \sigma e^{-\frac{r^2}{\sigma^2}}}{24r^2} \left(-e^{\frac{r^2}{\sigma^2}} \left[2\sqrt{\pi} \sigma^2 r^3 + 8\sigma^5 - 2\sqrt{\pi} \sigma^3 r^2 \operatorname{Erf} \left(\frac{r}{\sigma} \right) \right] + 8r^2 \sigma^3 + 8\sigma^5 \right) . \quad (12)$$

From the potential V we can evaluate E^i but we still need to specify a shape for the vector potential \mathcal{X}_r . The XCFC formalism assumes maximal slicing, $K = 0$, where K is the trace of the extrinsic curvature. Therefore, the evolution equation for the scalar potential takes the form

$$\partial_t \mathcal{X}_\phi = -\mathcal{X}^i D_i \alpha - \alpha D_i \mathcal{X}^i + \beta^\varphi \partial_\varphi \mathcal{X}_\phi , \quad (13)$$

where we have considered that the only non-zero component of the shift vector is β^φ , as in the scalar case. Using Eq. (10) we get

$$D_i (\alpha \mathcal{X}^i) = i(\omega + \beta^\varphi) \mathcal{X}_\phi , \quad (14)$$

which has the same form as (8) and can be solved similarly, yielding

$$\mathcal{X}^i = \frac{i}{\alpha} (\omega + \beta^\varphi) E^i . \quad (15)$$

Since \mathcal{X}^i can be written as the gradient of a potential function, it is an irrotational field. Therefore the ‘‘magnetic’’ field for these initial data is zero by construction.

As a summary, the $t = 0$ initial data for the fields read

$$\begin{aligned} \mathcal{X}_\phi(r, \theta, \varphi) &= A r^2 e^{-\frac{r^2}{\sigma^2}} \sin \theta e^{i\varphi} , \\ \hat{E}^r(r, \theta, \varphi) &= -\hat{E}^r(r, \theta) e^{i\varphi} , \\ E^\theta(r, \theta, \varphi) &= -\hat{E}^\theta(r, \theta) e^{i\varphi} , \\ E^\varphi(r, \theta, \varphi) &= -\hat{E}^\varphi(r, \theta) e^{i(\varphi+\pi/2)} , \\ \mathcal{X}_r(r, \theta, \varphi) &= \hat{\mathcal{X}}_r(r, \theta) e^{i(\varphi+\pi/2)} , \\ \mathcal{X}_\theta(r, \theta, \varphi) &= \hat{\mathcal{X}}_\theta(r, \theta) e^{i(\varphi+\pi/2)} , \\ \mathcal{X}_\varphi(r, \theta, \varphi) &= -\hat{\mathcal{X}}_\varphi(r, \theta) e^{i\varphi} , \end{aligned} \quad (16)$$

where the r and θ dependence is:

$$\hat{E}^r(r, \theta) = \frac{A \sigma^2}{12r^3} \left(8\sigma^4 - 2e^{-\frac{r^2}{\sigma^2}} [3r^4 + 4r^2 \sigma^2 + 4\sigma^4] - \sqrt{\pi} r^3 \sigma \operatorname{Erf} \left(\frac{r}{\sigma} \right) \right) \sin \theta , \quad (17)$$

$$\hat{E}^\theta(r, \theta) = \frac{A \sigma e^{-\frac{r^2}{\sigma^2}}}{24r^3} \left(-e^{\frac{r^2}{\sigma^2}} \left[2\sqrt{\pi} \sigma^2 r^3 + 8\sigma^5 - 2\sqrt{\pi} \sigma^3 r^2 \operatorname{Erf} \left(\frac{r}{\sigma} \right) \right] + 8r^2 \sigma^3 + 8\sigma^5 \right) \cos \theta , \quad (18)$$

$$\hat{E}^\varphi(r, \theta) = \frac{A \sigma e^{-\frac{r^2}{\sigma^2}}}{24r^3} \left(-e^{\frac{r^2}{\sigma^2}} \left[2\sqrt{\pi} \sigma^2 r^3 + 8\sigma^5 - 2\sqrt{\pi} \sigma^3 r^2 \operatorname{Erf} \left(\frac{r}{\sigma} \right) \right] + 8r^2 \sigma^3 + 8\sigma^5 \right) \cos \theta , \quad (19)$$

$$\hat{\mathcal{X}}_i(r, \theta) = \frac{1}{\alpha} (\omega + \beta^\varphi) \gamma_{ij} \hat{E}^j(r, \theta) . \quad (20)$$

Appendix B. Code Assessment. For the numerical evolutions we employ the codes introduced in Refs. [16, 31], which make use of the EINSTEINTOOLKIT infrastructure [28, 42, 43] with the CARPET package [44, 45] for mesh-refinement capabilities and AHFINDERDIRECT [46, 47] for finding apparent horizons. The evolution of the spacetime metric is handled either by LEAN [48] - originally presented in [49] for vacuum spacetimes, and now also distributed within the EINSTEINTOOLKIT infrastructure - or McLachlan [50].

The numerical code we have used to evolve the rotating Proca stars has been assessed in [30] for a real Proca field and in [16] for the complex case. In this section we will discuss the convergence analysis of the rotating Proca star stable solution. We performed the evolution of model 1_P with three different resolutions, namely with high resolution, corresponding to $\{(96, 48, 24, 12), (1.6, 0.8, 0.4, 0.2)\}$, medium resolution grid structure of $\{(96, 48, 24, 12), (3.2, 1.6, 0.8, 0.4)\}$ and low resolution $\{(96, 48, 24, 12), (6.4, 3.2, 1.6, 0.8)\}$. The first set of numbers indicates the spatial domain of each level and the second set indicates the resolution. In Fig. 5 we show the time evolution of the angular momentum for the different resolutions. The lower the resolution, the larger is the drift at $t = 1000$: 12.3% for low resolution, 2.3% for

medium resolution and 0.6% for the high resolution. The L1-norm can be rescaled to second order convergence as shown in the inset of Fig 5. For further details concerning the performance of the codes employed, please see [31, 48] for the scalar code and [16] for the Proca one.

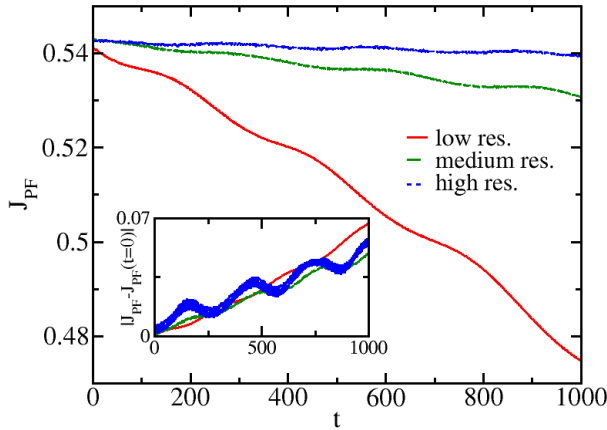


FIG. 5: Time evolution of the angular momentum of model 1P for three different resolutions. (Inset) The L1-norm rescaled to second order convergence.

- [1] B. P. Abbott et al. (LIGO Scientific, Virgo) (2018), 1811.12907.
- [2] Gravity Collaboration, R. Abuter, A. Amorim, M. Bauböck, J. P. Berger, H. Bonnet, W. Brandner, Y. Clénet, V. Coudé Du Foresto, and P. T. de Zeeuw, *Astron. Astrophys.* **618**, L10 (2018), 1810.12641.
- [3] K. Akiyama et al. (Event Horizon Telescope), *Astrophys. J.* **875**, L1 (2019).
- [4] D. J. Kaup, *Phys. Rev.* **172**, 1331 (1968).
- [5] R. Ruffini and S. Bonazzola, *Phys. Rev.* **187**, 1767 (1969).
- [6] R. Brito, V. Cardoso, C. A. R. Herdeiro, and E. Radu, *Phys. Lett.* **B752**, 291 (2016), 1508.05395.
- [7] E. Seidel and W.-M. Suen, *Phys. Rev. Lett.* **72**, 2516 (1994), gr-qc/9309015.
- [8] F. Di Giovanni, N. Sanchis-Gual, C. A. R. Herdeiro, and J. A. Font, *Phys. Rev.* **D98**, 064044 (2018), 1803.04802.
- [9] M. Gleiser and R. Watkins, *Nucl. Phys.* **B319**, 733 (1989).
- [10] T. D. Lee and Y. Pang, *Nucl. Phys.* **B315**, 477 (1989), [129(1988)].
- [11] N. Sanchis-Gual, C. Herdeiro, E. Radu, J. C. Degollado, and J. A. Font, *Phys. Rev. D* **95**, 104028 (2017).
- [12] F. E. Schunck and E. W. Mielke, *Class. Quant. Grav.* **20**, R301 (2003), 0801.0307.
- [13] S. L. Liebling and C. Palenzuela, *Living Rev. Rel.* **15**, 6 (2012), 1202.5809.
- [14] C. Palenzuela, I. Olabarrieta, L. Lehner, and S. L. Liebling, *Physical Review D* **75**, 064005 (2007).
- [15] C. Palenzuela, L. Lehner, and S. L. Liebling, *Physical Review D* **77**, 044036 (2008).
- [16] N. Sanchis-Gual, C. Herdeiro, J. A. Font, E. Radu, and F. Di Giovanni, *Phys. Rev. D* **99**, 024017 (2019).
- [17] F. E. Schunck and E. W. Mielke, *Phys. Lett.* **A249**, 389 (1998).
- [18] S. Yoshida and Y. Eriguchi, *Phys. Rev.* **D56**, 762 (1997).
- [19] B. Kleihaus, J. Kunz, M. List, and I. Schaffer, *Phys. Rev.* **D77**, 064025 (2008), 0712.3742.
- [20] C. Herdeiro, E. Radu, and H. Runarsson, *Class. Quant. Grav.* **33**, 154001 (2016), 1603.02687.
- [21] F. H. Vincent, Z. Meliani, P. Grandclement, E.ourgoulhon, and O. Straub, *Class. Quant. Grav.* **33**, 105015 (2016), 1510.04170.
- [22] Z. Meliani, F. H. Vincent, P. Grandclement, E.ourgoulhon, R. Monceau-Baroux, and O. Straub, *Class. Quant. Grav.* **32**, 235022 (2015), 1510.04191.
- [23] C. A. R. Herdeiro and E. Radu, *Phys.Rev.Lett.* **112**, 221101 (2014), 1403.2757.
- [24] P. Grandclement, C. Somé, and E.ourgoulhon, *Phys. Rev.* **D90**, 024068 (2014), 1405.4837.
- [25] C. Herdeiro and E. Radu, *Class. Quant. Grav.* **32**, 144001 (2015), 1501.04319.
- [26] C. A. R. Herdeiro and E. Radu, *Phys. Rev. Lett.* **119**, 261101 (2017), 1706.06597.
- [27] C. Herdeiro, I. Perapechka, E. Radu, and Ya. Shnir (2019), 1906.05386.
- [28] EinsteinToolkit, *Einstein Toolkit: Open software for relativistic astrophysics*, <http://einstein toolkit.org/>.
- [29] F. Löffler, *Classical Quantum Gravity* **29**, 115001 (2012).
- [30] M. Zilhão, H. Witek, and V. Cardoso, *Class. Quant. Grav.* **32**, 234003 (2015), 1505.00797.
- [31] P. V. P. Cunha, J. A. Font, C. Herdeiro, E. Radu, N. Sanchis-Gual, and M. Zilhão, *Phys. Rev.* **D96**, 104040 (2017), 1709.06118.
- [32] V. Paschalidis and N. Stergioulas, *Living Rev. Rel.* **20**, 7 (2017), 1612.03050.
- [33] M. Saijo, T. W. Baumgarte, and S. L. Shapiro, *Astrophys. J.* **595**, 352 (2003), astro-ph/0302436.
- [34] A. L. Watts, N. Andersson, and D. I. Jones, *Astrophys. J.* **618**, L37 (2005), astro-ph/0309554.
- [35] B. Zink, N. Stergioulas, I. Hawke, C. D. Ott, E. Schnetter, and E. Muller, *Phys. Rev. Lett.* **96**, 161101 (2006), gr-qc/0501080.
- [36] B. Zink, N. Stergioulas, I. Hawke, C. D. Ott, E. Schnetter, and E. Mueller, *Phys. Rev.* **D76**, 024019 (2007), astro-ph/0611601.
- [37] K. Kiuchi, M. Shibata, P. J. Montero, and J. A. Font, *Phys. Rev. Lett.* **106**, 251102 (2011), 1105.5035.
- [38] M. Bezares, C. Palenzuela, and C. Bona, *Phys. Rev.* **D95**, 124005 (2017), 1705.01071.
- [39] C. Palenzuela, P. Pani, M. Bezares, V. Cardoso, L. Lehner, and S. Liebling, *Phys. Rev. D* **96**, 104058 (2017).
- [40] I. Cordero-Carrion, P. Cerda-Duran, H. Dimmelmeier, J. L. Jaramillo, J. Novak, and E.ourgoulhon, *Phys. Rev.* **D79**, 024017 (2009), 0809.2325.
- [41] H. Okawa, H. Witek, and V. Cardoso, *Phys.Rev.* **D89**, 104032 (2014), 1401.1548.
- [42] F. Löffler, J. Faber, E. Bentevegna, T. Bode, P. Diener, et al., *Class.Quant.Grav.* **29**, 115001 (2012), 1111.3344.
- [43] M. Zilhão and F. Löffler, *Int.J.Mod.Phys.* **A28**, 1340014 (2013), 1305.5299.
- [44] E. Schnetter, S. H. Hawley, and I. Hawke, *Class. Quant. Grav.* **21**, 1465 (2004), gr-qc/0310042.
- [45] Carpet, <http://www.carpetcode.org/>, Carpet: Adap-

- tive Mesh Refinement for the Cactus Framework.
- [46] J. Thornburg, *Class. Quant. Grav.* **21**, 743 (2004), [gr-qc/0306056](#).
 - [47] J. Thornburg, *Phys. Rev.* **D54**, 4899 (1996), [gr-qc/9508014](#).
 - [48] H. Witek and M. Zilhão, CANUDA, <https://bitbucket.org/canuda/>.
 - [49] U. Sperhake, *Phys. Rev.* **D76**, 104015 (2007), [gr-qc/0606079](#).
 - [50] J. D. Brown, P. Diener, O. Sarbach, E. Schnetter, and M. Tiglio, *Phys. Rev. D* **79**, 044023 (2009), [arXiv:0809.3533 \[gr-qc\]](#).
 - [51] The energy and angular momentum densities are the ones defined from the Komar integrals, as in [16, 31].